Highly Bendable Large-Area Printed Bulk Heterojunction Film Prepared by the Self-Seeded Growth of Poly(3-hexylthiophene) Nanofibrils

10 AUTHORS, INCLUDING:

Tae Il Lee
Yonsei University
107 PUBLICATIONS **918** CITATIONS

SEE PROFILE

Jae-Wook Kang
Chonbuk National University
121 PUBLICATIONS **4,349** CITATIONS

SEE PROFILE

Unyong Jeong
Pohang University of Science and Technology
144 PUBLICATIONS **4,756** CITATIONS

SEE PROFILE

Highly Bendable Large-Area Printed Bulk Heterojunction Film Prepared by the Self-Seeded Growth of Poly(3-hexylthiophene) Nanofibrils

Jin Young Oh,[†] Minkwan Shin,[†] Tae Il Lee,[†] Woo Soon Jang,[†] Yu-Jeong Lee,[†] Chang Su Kim,[‡] Jae-Wook Kang,[§] Jae-Min Myoung,[†] Hong Koo Baik,*,[†] and Unyong Jeong*,[†]

[†]Department of Materials Science and Engineering, Yonsei University, 134 Shinchong-dong, Seoul 120-750, Republic Korea
[‡]Advanced Functional Thin Films Department, Korea Institute of Materials Science, Changwon 641-831, Republic of Korea
[§]Department of Flexible and Printable Electronics, Chonbuk National University, Jeonju 561-756, Republic of Korea

Ⓢ *Supporting Information*

ABSTRACT: Applying conventional printing technologies to fabricate large-area flexible bulk heterojunction (BHJ) solar cells is of great interest. Achieving this task requires (i) large tolerance of the maximum photoconversion efficiency (PCE) to the film thickness, (ii) fast hole transport in both the thickness and lateral directions of the BHJ layer, and (iii) improved stability against bending and heat. This paper demonstrates that a P3HT:PCBM BHJ layer made of long P3HT nanofibrils of almost 100% crystallinity can be an excellent approach to achieve large-area printed solar cells. We applied a cool-and-heat

(C&H) process with a P3HT/PCBM *m*-xylene solution to generate P3HT:PCBM nanofibril composite films. We found that the hole transport of the nanofibril composite was 2.6 times faster in the thickness direction and 6.5 times more conductive in the in-plane direction compared with conventionally annealed composites. The fast hole transport in the thickness direction led to negligible dependence of the PCE on the thickness of the composite layer. The improved conductivity in the in-plane direction prevented the sharp drop of the PCE as the active area increased. Taking advantage of the unique characteristics, we employed a roll-printing method to fabricate large-area unit solar cells in air. In addition, the curved contour path of the nanofibrils provided excellent stability against large bending strains, allowing the production of highly bendable organic solar cells.
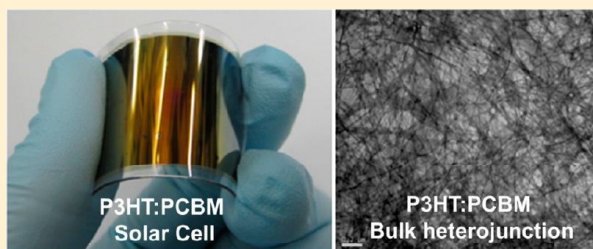
■ INTRODUCTION

The need for flexible low-cost photovoltaic devices has attracted intensive interest in polymer-based organic solar cells.[1−3] Typical polymer solar cells consist of a conjugated polymer donor and the fullerene derivative acceptor. The development of the bulk heterojunction (BHJ) as a light-absorbing layer made it possible to overcome the relatively small rate of charge separation which is caused by the strong binding energy of the electron−hole pair in polymer semi-conductors.[4,5] BHJ solar cells made of polythiophene-based polymer, including regioregular poly(3-hexylthiophene) (P3HT) and copolymer, and [6,6]-phenyl-C_{61}-butyric acid methyl ester (PCBM) resulted in the power conversion efficiency (PCE) in the range 3−5%.[6,7] In addition, polythiophene-based block copolymers have also been studied to improve performance of the device.[8−10] Very recently, the use of low-band-gap semiconducting polymers and modified fullerene derivatives led to the PCE of 10%.[11−13] Another remarkable advantage of the BHJ solar cells lies in the solution process, which is readily adaptable to conventional printing techniques.[14] The compatibility with printed BHJ layer to the plastic substrates may allow the production of highly flexible solar cells.[15]

In spite of the recent advances in PCE with low-band-gap polymers, P3HT/PCBM BHJ solar cells continue to be studied actively. But, the current P3HT/PCBM BHJ films have several shortcomings that are not appropriate for large-area printing. First, the optimized thickness (∼100 nm) of the BHJ layer is not compatible with the thicknesses routinely obtained by current printing technologies (300−600 nm).[16] Second, the size of a unit cell with a good PCE is too small, which eventually causes the PCE to decline considerably in a large module. The dimensional limitation in the solar cell design is mainly caused by the low hole mobility through the polymer phase compared to the electron mobility through the PCBM phase. Hole−electron recombinations become severe as the contour length of the charges becomes longer. Third, the post-treatment by heat or solvent[17−19] should be omitted to take full advantage of the continuous printing process. Although the post-treatment increases the crystallinity of the P3HT and refines the interface between the donor and acceptor phases, the macrophase separation of the PCBM takes place and

Scheme 1. Schematic Illustration of the Cooling-and-Heating (C&H) Process of the P3HT/PCBM Solution and the Roll-Printing Process Used To Fabricate Large-Area Unit Cells[a]
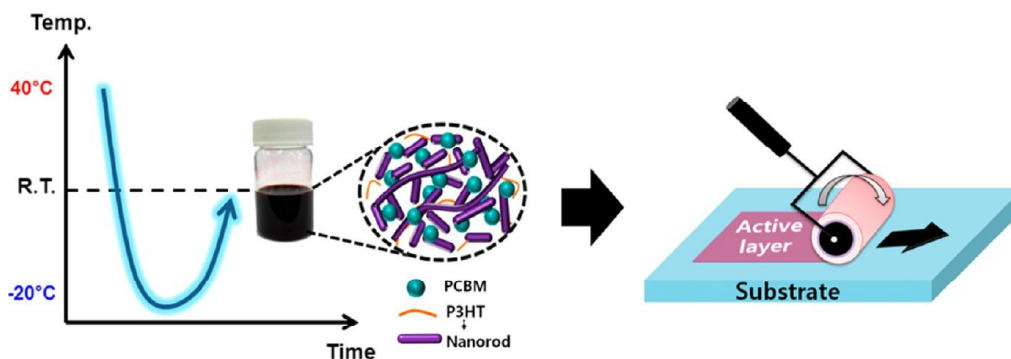
[a]After the C&H process, the solution contains P3HT nanorods that serve as seeds for the rapid growth of P3HT crystals into the nanofibrils during the coating process.

decreases the fill factor (FF) of the solar cells.[20−24] Also, the electrical properties of the BHJ layer are not stable under bending strains. When the stress is accumulated in the high-modulus P3HT/PCBM BHJ layer, defects and cracks can nucleate and propagate so that the PCE can sharply drop. Finally, conventional P3HT/PCBM thin films are very weak against heat mainly due to the aggregation of the PCBM even at temperatures below 100 °C.[25−28]

In this study, we employed a BHJ layer consisting of long P3HT nanofibrils and PCBM to overcome the aforementioned shortcomings. P3HT nanofibrils are advantageous in several ways.[29−38] They allow faster hole transport through $\pi−\pi$ stacking aligned in the longitudinal direction, which may impart more tolerance to thickness optimization processes and which may also increase the size of unit cells without a severe loss of efficiency. In addition, no postannealing is required if the crystallinity of P3HT is close to 100% in these types of coated films. Finally, they offer superior absorption of external mechanical strain owing to the curvy contour path of the nanofibrils as well as enhanced thermal stability of the BHJ layer due to the restricted movement of the PCBM, as the PCBM is confined in the P3HT nanofibril network.

Very recently, we reported a straightforward coating process to prepare P3HT nanofibril films with almost 100% crystallinity.[39] We cooled a *m*-xylene or *p*-xylene P3HT solution to −15 °C and then heated the solution to room temperature. After the cooling-and-heating (C&H) cycle, the solution contained P3HT nanorods that acted as seeds for the rapid growth of P3HT crystals into the nanofibrils during a spin-coating process. In this study, we extended this process to the conventional roll printing and produced large-area annealing-free solar cells having improved levels of stability to bending and heating.

■ RESULTS AND DISCUSSION

Scheme 1 shows the overall process used to produce the nanofibril-based solar cells. P3HT and PCBM were dissolved in *m*-xylene (1:1 (w/w), 2 wt % in total) at 40 °C. The solution was cooled in a chiller at −15 °C for 15 min and then heated to room temperature (25 °C) in air. In previous research,[39] we found that P3HT crystals grow into nanofibrils longer than 10 μm in such a solution during cooling. After heating to room temperature, the nanofibrils were partially dissolved, but nanorods of submicrometer length remained in the solution.

The stability of the P3HT nanorods at room temperature is indebted to dissociation energy of crystals, which is the activation energy barrier required to dissolve crystallized materials. Because the dissociation is a thermodynamic phenomenon, the P3HT nanorods are stable as long as the temperature is maintained at or below room temperature.[39,40] The crystal nanorods serve as seeds for nanofibril growth during the coating process. Unlike P3HT, PCBM is stably dissolved in the solution during the C&H cycle and did not affect the growth of the P3HT nanofibrils. To fabricate solar cells, the solution was spin-coated or roll-printed on ITO substrate or Au-evaporated PET substrates. PEDOT:PSS was spin-coated before coating with the BHJ layer. The counter electrode (LiF/Al) was thermally evaporated on the BHJ layer. The solar cells did not require thermal or solvent annealing as nearly 100% crystallinity of the P3HT was achieved during the coating process.[39]

Supporting Information Figure S1a−c shows the UV−vis absorbance spectra of the P3HT/PCBM solution and film. The amorphous solution or film without the C&H cycle was labeled as "conventional" while the solution or film after the C&H cycle was labeled as "C&H". Contrary to the conventional solution and film, the C&H solution and film exhibited a significant red-shift and increasing shoulder peak, which indicates improving the 1D self-assembly of P3HT chains by $\pi−\pi$ stacking.[41] The crystallinity of P3HT in the C&H film was calculated to be ≥95% from the peak position of P_1.[39] A full discussion of Figure S1 is described in the Supporting Information. The UV−vis absorbance of the P3HT/PCBM solution after the simple C&H process was identical to that of the P3HT solution after the C&H process without PCBM. The spectra are compared in Figure S2, and the X-ray diffraction results of the films are shown in Figure S3.

The degree of $\pi−\pi$ stacking induced by the 1D crystal growth is directly related to the optical bandgap (E_g). E_g is expressed as a function of the absorption coefficient (α) and photon energy ($h\nu$) with the relationship $(\alpha h\nu)^2 = A(h\nu − E_g)$, where A is a constant. The absorption coefficient (α) is quantified as $\alpha = [\ln(1/T)]/D$, where T is the transmittance and D is the thickness of the active layer. Thus, E_g is determined by extrapolating the linear region in the plot of $(\alpha h\nu)^2$ versus the photon energy and then using the intersection on the horizontal axis. Figure 1a,b shows a plot $(\alpha h\nu)^2$ versus $h\nu$ of the solutions and films from the UV−vis
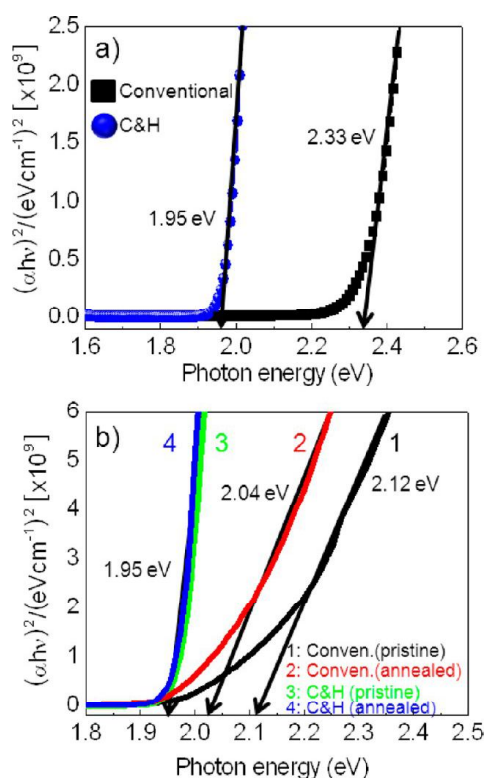
Figure 1. Diagrams of $(\alpha h\nu)^2$ vs $h\nu$ from the P3HT/PCBM solutions (a) and their thin films (b). The term "conventional" means an amorphous solution or thin film coated in an amorphous state. The "C&H" indicates solution or films prepared by the cooling-and-heating (C&H) process. The terms "pristine" and "annealed" refer to the as-coated films and the thermally annealed films, respectively.

transmittance spectra. E_g in the conventional solution was 2.33 eV, which was lowered to 2.12 eV after the spin-coating process. Thermal annealing of the film further decreased E_g to 2.04 eV. In contrast to the changes of E_g in the conventional process, the E_g values in the C&H process were identical (1.95 eV) in the solution, in the film without thermal annealing, and in the film after thermal annealing.

Figure 2 shows SEM and TEM images presenting the morphology of the C&H films of the pure nanofibrils (a, c) and the nanofibril/PCBM composite (b, d) which were directly spin-coated onto TEM grids. The 10 nm thick P3HT nanofibrils were distributed homogeneously and formed a physical network in both conditions. In previous research,[39] we found that the as-coated P3HT nanofibrils obtained by the C&H process were longer than 10 μm and that the layer spacing of the (001) plane was narrower than the one of the conventionally annealed films.

Figure 3 compares the characteristics of the photovoltaic cells prepared by the conventional process and the C&H process with/without thermal annealing. The values are summarized in Table 1. Figure 3a describes the structure of the cells. The thickness of the active layer was 150 nm, and the device area was 5.4 mm². As shown in Figure 3b, the $J–V$ curve of the pristine conventional film was far from an ideal curve, while the pristine C&H film showed a curve of the type typically found in thermally annealed P3HT/PCBM solar cells. The open-circuit voltage (V_{oc}) of the pristine C&H cell was lower than that of the conventionally annealed films. This can be explained by the

lowered bandgap (E_g) of the P3HT crystals (see Figure 1). The upshifted highest occupied molecular orbital (HOMO) level of the P3HT crystals might reduce the gap from the lowest unoccupied molecular orbital (LUMO) level of the PCBM phase. The loss of V_{oc} in the C&H cells was compromised by increase of the short-circuit current density (J_{sc}) and the fill factor (FF). The improved J_{sc} is attributed to the effective hole transport through the well-developed $\pi–\pi$ stacking of the P3HT nanofibrils. Previous work revealed that the rodlike P3HT crystals generated by coating on a cold substrate facilitated nanoscale homogeneous mixing with the PCBM phase and restricted the aggregation of the PCBM, which is often encountered in conventional films during thermal annealing.[41] Such a morphological advantage contributed to the improvement of the FF value so that the pristine C&H films had a better PCE (3.44%) than the conventional thermally annealed films (3.09%). The PCE of the C&H films was further increased to 3.82% by thermal annealing.

To realize printed solar cells, the optimal thickness of the coating layer should exceed that in the current condition (~100 nm) in the conventional spin-coating process. The absorbance of solar light increases as the thickness of the absorber layer increases, but the recombination of the charges also becomes severe due to the longer path for charge transport and the lower hole mobility compared to the electron mobility.[34,42,43] This trade-off determines the optimal thickness for the best PCE. The fast hole transport in the long nanofibrils may counterbalance the increased recombination, which would then increase the optimum thickness of the active layer of the solar cells.

We measured the hole and electron mobility levels in the 150 nm thick BHJ layer by employing the Mott−Gurney law as defined by the space charge limited current (SCLC) theory, $J_{SCLC} = 9\varepsilon_0\varepsilon_r\mu(V^2/L^3)$, where ε_0 and ε_r are respectively the permittivity in a vacuum and in the polymer layer, μ is the carrier mobility, and L is the thickness of the composite layer. Figures 4a and 4b correspondingly show the $J–V$ curves of a hole-only device (structure: Au/BHJ/Au) and an electron-only device (structure: Al/BHJ/Al). The electrode sets selectively allow the transport of holes or electrons due to the work function of the metals.[34] The electron and hole mobilities calculated from the SCLC region ($J \propto V^2$) are summarized in Table 2. The electron mobilities (μ_e) of the conventionally annealed film and the C&H film were similar, while the hole mobilities (μ_h) showed a considerable amount of dependence on the preparation condition. The hole mobility of the pristine C&H film was 2.6-fold greater than that of the conventional thermally annealed film. The hole mobility of the annealed C&H film was 3.4-fold higher than the conventional film, which is a distinct feature of the crystalline nanofibrils compared to conventional film.[34] Because of the enhanced hole mobility, the hole/electron mobility ratio (μ_e/μ_h) of the C&H films was significantly lowered (1.6−1.9), while the ratio of the conventional films was about 6.

In order to check the conducting capability of the nanofibril films, the current density of the nanofibril P3HT films in the thickness direction was compared with those of the conventionally annealed P3HT films. The P3HT films were spin-coated on a thermally evaporated Au electrode on a Si wafer, and another Au layer was evaporated on top of the P3HT films. We obtained $J–V$ curves of the P3HT films and extracted the electrical properties from the $J–V$ curves. The thickness of P3HT films was controlled by increasing the concentration of
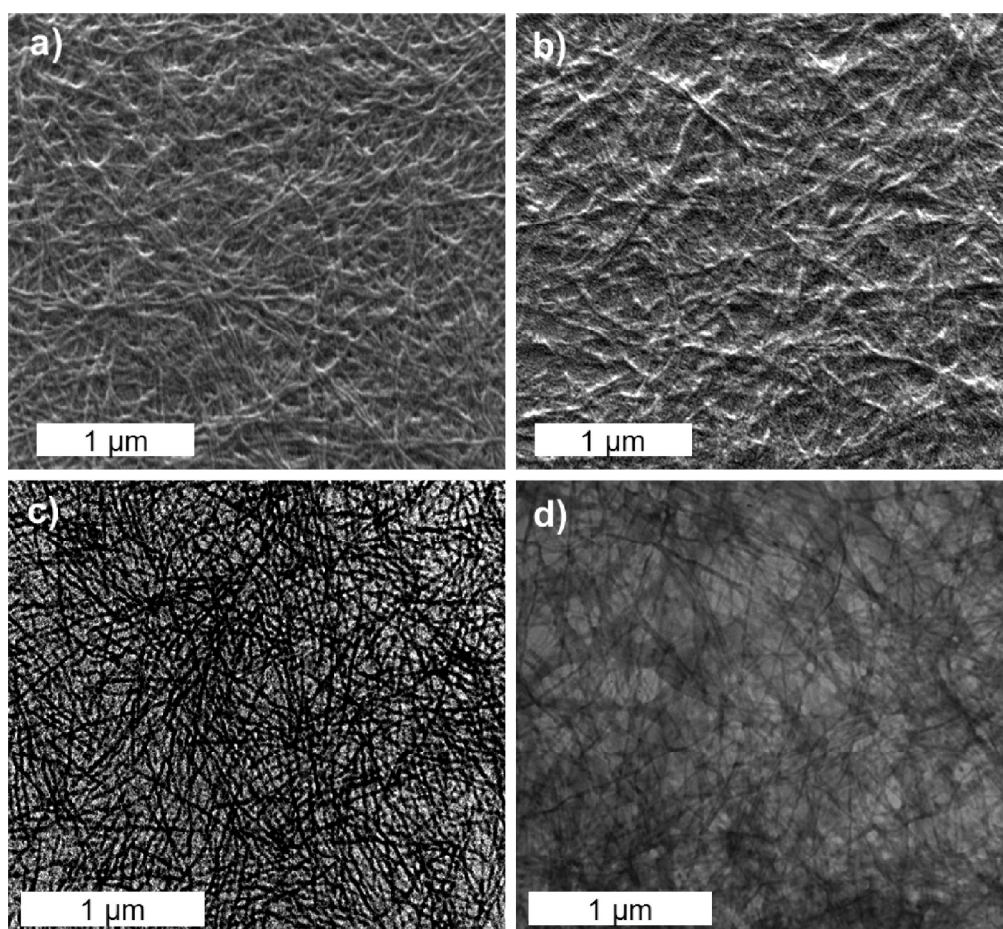
Figure 2. SEM and TEM images respectively of (a, c) P3HT nanofibrils and (b, d) P3HT nanofibrils:PCBM composite film prepared by directly coating the C&H solution onto a copper grid.
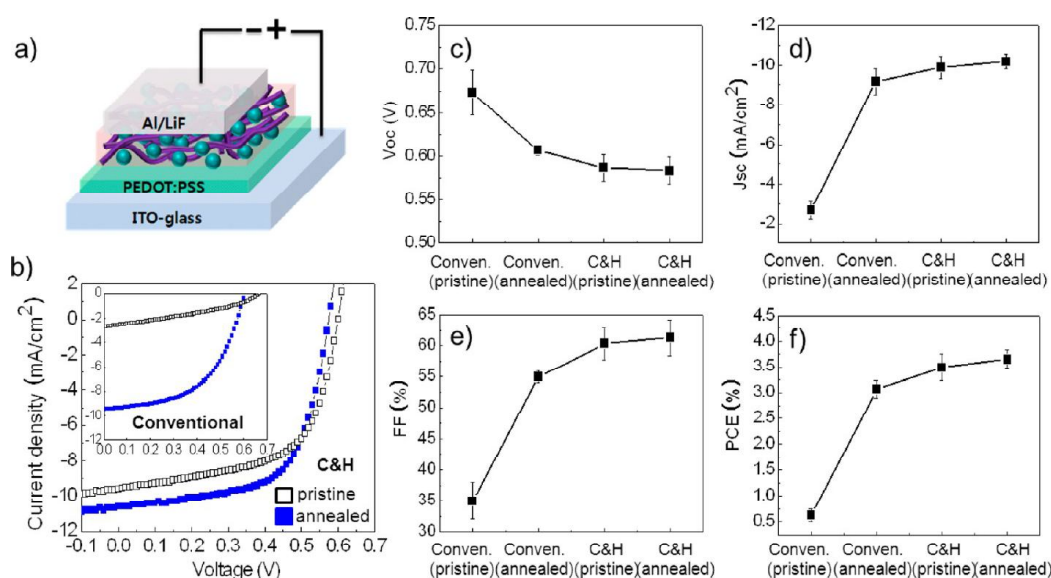

Figure 3. (a) Structure of the solar cells fabricated in this study. (b) Representative $J-V$ curves of solar cells prepared by the C&H process. The hollow square and the blue solid square correspond to the conditions before and after thermal annealing. The inset is the $J-V$ curves of the conventional solar cells before and after thermal annealing. (c–f) Photovoltaic characteristics of the solar cells according to the preparation process. (c) Open-circuit voltage (V_{oc}), (d) short-circuits current (J_{sc}), (e) fill factor (FF), and (f) photoconversion efficiency (PCE).

Table 1. Representative Photovoltaic Properties of BHJ Solar Cells as a Function of the Type of Photoactive Layer[a]

| type of film	condition	V_{oc} [V]	J_{sc} [mA/cm^2]	FF [%]	PCE [%]
conventional	pristine	0.67	−2.71	35	0.633
	annealed	0.60	−9.46	54	3.092
C&H	pristine	0.60	−9.6	60	3.444
	annealed	0.57	−10.63	63	3.825

[a]V_{oc}: open-circuit voltage; J_{sc}: short-circuit voltage; FF: fill factor; PCE: power conversion efficiency.
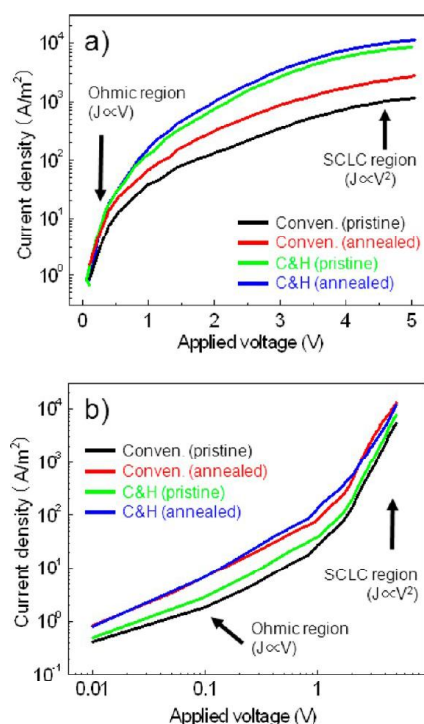
Figure 4. Current density−voltage (J−V) curves of the P3HT:PCBM composite films in the dark for a hole-only device (Au/BHJ/Au) (a) and an electron-only device (Al/BHJ/Al) (b).

Table 2. Charge Carrier Mobility of P3HT:PCBM Blended Films as a Function of the Type of Film[a]

type of film	condition	μ_e [cm^2/V·s]	μ_h [cm^2/V·s]	μ_e/μ_h
conventional	pristine	4.27×10^{-4}	7.50×10^{-5}	5.69
	annealed	1.00×10^{-3}	1.45×10^{-4}	6.89
C&H	pristine	6.10×10^{-4}	3.76×10^{-4}	1.62
	annealed	9.50×10^{-4}	5.00×10^{-4}	1.90

[a]μ_e: electron mobility; μ_h: hole mobility.

solution. Figure 5a,b represents the current densities of the conventional films (a) and the nanofibril films caused by the C&H process (b) as the film thickness was increased. Thick films (≥300 nm) were prepared by a roll-printing process. Roll-printing the polymer solution produced large-area uniform films. The C&H films exhibit a considerably higher current density than the conventionally annealed film at the same thickness. Figure 5c exhibits the changes in the resistance vs thickness as obtained from the I−V curves. The slopes of the conventional films and the C&H films were 0.046 and 0.017, respectively, which indicates that the resistance of the C&H films is 2.7 times less sensitive to the film thickness compared
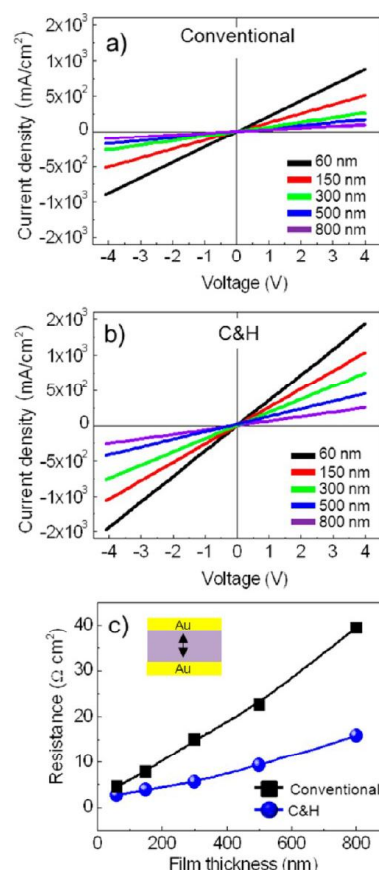
Figure 5. (a, b) J−V curves of the pure P3HT films in the dark for solar cells prepared by the conventional coating process (a) and by the C&H process (b). (c) Resistance change of the P3HT film as a function of the film thickness. The hole conductance was measured by the Au/BHJ/Au electrode.

to the conventional films, which is consistent with the mobility increase.

The reduced thickness dependence of the hole transport in the C&H films leads to greater tolerance at the optimum thickness of the solar cells, which can be critical in large-area printing applications. Figure 6 exhibits the J−V curves of the solar cells formulated from the conventional films (a) and the C&H films (b). The devices were fabricated in air, except for the evaporation of the Al electrode. Thin films were made by spin-coating and thick films (≥300 nm) were prepared by roll-printing. The conventional film devices were thermally annealed at 150 °C for 10 min, but the C&H films were not. The active area of the cells was 5.4 mm^2. When the film thickness of the conventionally annealed film was 60 nm, the current density was low (−6.41 mA/cm^2) due to the small amount of light absorption. Increasing the thickness to 150 nm, the J_{sc} value increased to −9.57 mA/cm^2 (Figure 6a). However, J_{sc} and FF monotonically decreased as the film thickness was further increased (300, 500, and 800 nm). Figure 6b shows the J−V curves of the solar cells made with the C&H film. As expected, V_{oc} was lower but J_{sc} was higher than the conventional cells. In contrast to the conventional cells, J_{sc} of the C&H solar cells increased as the thickness of the active layer was increased to 500 nm. This is explained by the increased exciton generation in the thicker active layer. The
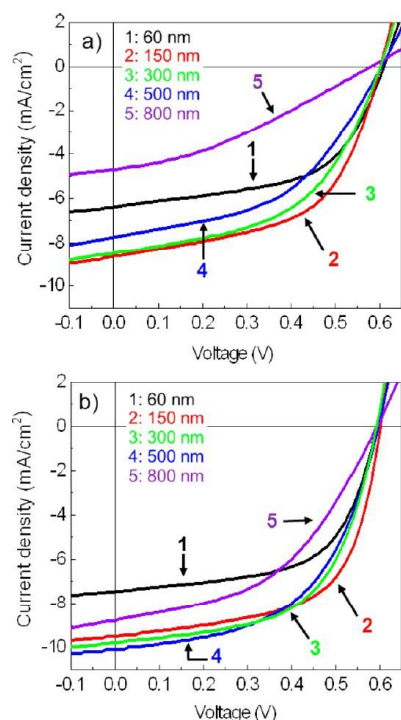
Figure 6. Dependence of the $J{-}V$ curves on the thickness of the BHJ layer prepared by the conventional coating process (a) and by the C&H process (b).

solar cells with the 800 nm thick active layer still showed a slight degradation in the value of J_{sc}. The solar cell characteristics according to the thickness of the active layer are summarized in Table 3. The PCE values of the cells made

Table 3. Representative Photovoltaic Properties of P3HT Nanofibril−PCBM Blended Films (Photoactive Layer) as a Function of Their Thickness

type of film	film thickness (nm)	V_{oc} [V]	J_{sc} [mA/cm^2]	FF [%]	R_s [Ω·cm^2]	PCE [%]
conventional	60	0.61	−6.41	55	16.95	2.167
	150	0.60	−9.57	53	13.48	3.070
	300	0.60	−8.50	51	15.38	2.588
	500	0.60	−9.76	48	26.86	2.226
	800	0.58	−4.71	33	87.50	0.905
C&H	60	0.59	−7.46	60	9.46	2.642
	150	0.60	−9.51	61	6.82	3.473
	300	0.59	−9.81	58	9.57	3.354
	500	0.60	−10.10	53	11.84	3.214
	800	0.59	−8.78	47	24.17	2.410

with the C&H films were similar in the thickness range of 150 and 500 nm, while the PCE of the conventional cells was exclusively optimized at ∼150 nm.

Fabrication of large-area unit cells is critical for the industrialization of organic solar cells because the conversion efficiency of device sharply drops as the active area increases. Loss of performance in large active area device is one of the major concerns for industrializing organic solar cells, and there are two main factors to decrease the efficiency: resistance of electrode and resistance of the active layer. While a lot of approaches to improve the resistance of electrode have been

introduced, the study to reduce resistance of the active layer has not been investigated very well. The current path in the conventional BHJ film is complicated and not directly vertical,[44−48] which causes the increase of resistance. Introducing long P3HT nanofibrils may mitigate this drawback. To confirm the advantage of P3HT nanofibril, the in-plane current density of the nanofibril film was examined. Figure 7 shows the
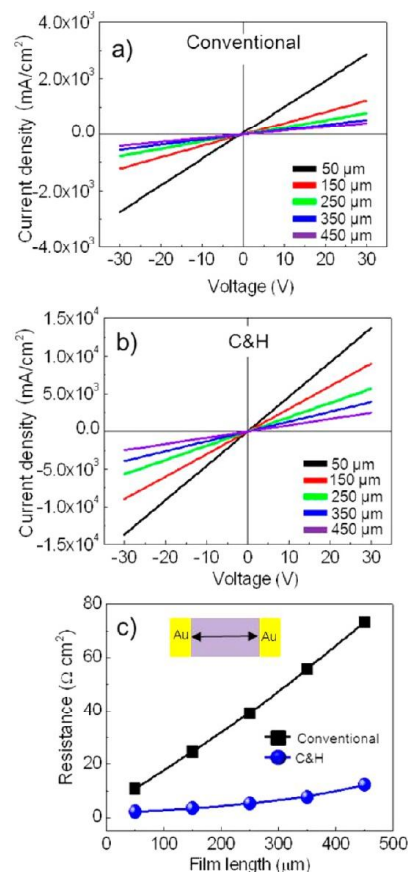

Figure 7. (a, b) $J{-}V$ curves of pure P3HT films in the dark for solar cells prepared by the conventional coating process (a) and by the C&H process (b). (c) Resistance change of the P3HT film as a function of the measuring distance. The hole conductance was measured by the Au/BHJ/Au electrode.

current densities of the conventional films (a) and the nanofibril films created by the C&H process (b) as the measuring distance was varied. The film thicknesses are identical (20 nm). The C&H films exhibit substantially higher current density level compared to the conventionally annealed film at the same length. Figure 7c represents the changes in the resistance vs the measuring distance. The slopes of the conventional films and the C&H films were 0.156 and 0.024, respectively, which indicates that the in-plane resistance of the C&H films is smaller by 6.5 times. These results strongly support the contention that BHJ with P3HT nanofibril is more suitable for large-area solar cells than BHJ with conventional film.

The enhanced mobility of the holes and the greater PCE tolerance to the thickness allowed us to apply the conventional printing technologies for the creation of large-area unit cells, as shown in the inset of Figure 8 (active area = 10.5 cm^2). The
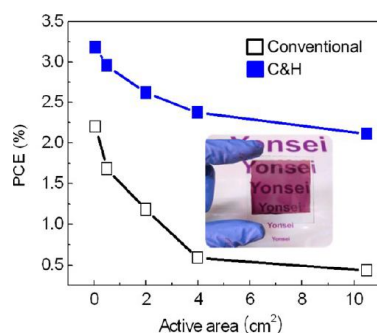
Figure 8. Changes of the photoconversion efficiency (PCE) as a function of the active area of the solar cells. The inset is a photograph of the solar cell fabricated by roll-printing. The active area of the solar cell in the inset was 10.5 cm^2.

active layers were coated by roll-printing in air.[49] Figure 8 shows the change in the PCE as the active area is increased. The thicknesses were fixed at ∼300 nm in this case. In the

conventional solar cells, the PCE dropped abruptly as the photoactive area was increased, dropping to 0.43% with an active layer that was 10.5 cm^2 wide. Meanwhile, the PCE of the nanofibril-based cells showed much less of a drop while maintaining 2.1% PCE with a 10.5 cm^2 active layer.

One of the potential advantages of polymer solar cells is their bendable characteristic. However, the spin-coated P3HT thin films are known to be weak against external strain. The electrical conductance and field effect mobility of them sharply decrease, even at small strains.[49−52] A few groups have tried to design better structures to relieve mechanical stress.[53−55] Recently, Kim et al. reported improved tolerance by introducing a wrinkled surface in a device.[54] The prewrinkled surface absorbed the bending stress. However, previous studies did not focus on the simple and inexpensive production of solar cells. We hold that the curvy contour path of the nanofibrils can effectively absorb external strain. Figure 9 compares the solar cell characteristics depending on the bending radius. A poly(ethylene terephthalate) (PET) film with a thickness of 180 μm was used as the plastic substrate. Given that brittle ITO
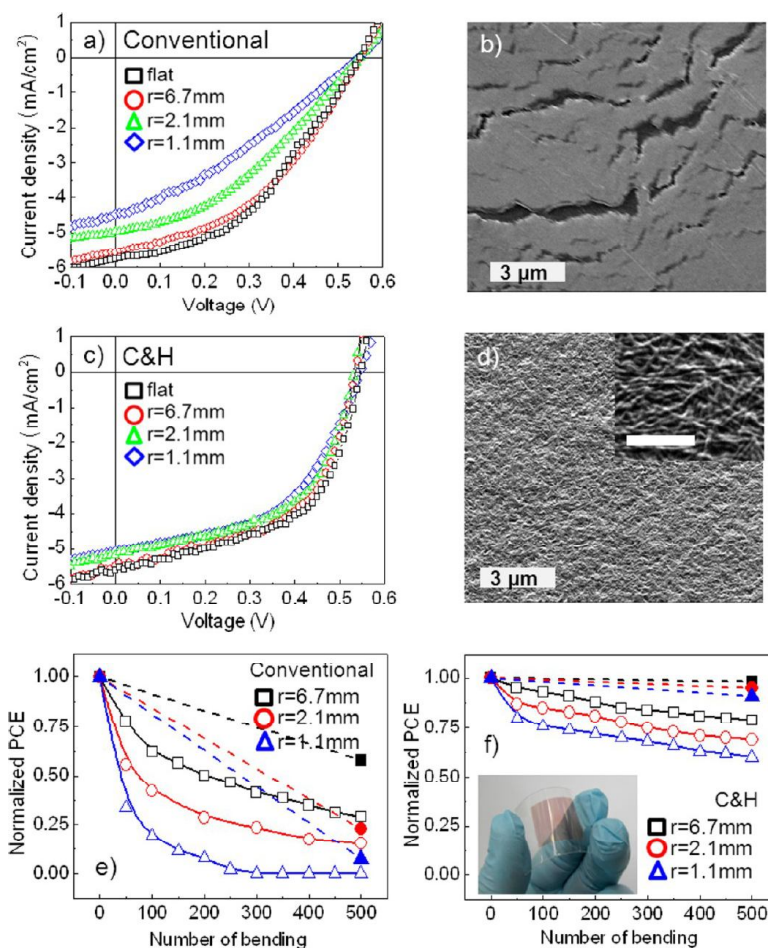

Figure 9. Solar cell characteristics according to a bending test. The bending radii (r) are given in each graph. An ITO electrode was replaced by Au (10 nm thickness) on a PET substrate. (a, b) J−V curves of the conventionally annealed solar cells and a SEM image of the BHJ layer with a small bending radius (r = 1.1 mm). (c, d) J−V curves of C&H solar cells and a SEM image of the BHJ layer with a small bending radius (r = 1.1 mm). The scale bar of the inset is 300 nm. (e) Normalized PCE of conventionally annealed solar cells during repeated bending events. (f) Normalized PCE of C&H solar cells during repeated bending events. The solid symbols in (e) and (f) represent the normalized PCEs with the BHJ films that were 500 times bent with the same bending radii on a PDMS substrate: r = 6.7 mm (■), r = 2.1 mm (●), and r = 1.1 mm (▲). The tests were conducted to remove the effect of electrodes. The dotted lines are simple guides to the eyes.

is very weak under strain, we used an Au layer (10 nm in thickness) as the electrode. Au was thermally evaporated onto PET substrate, and then PEDOT:PSS was spin-coated onto it.[54] The BHJ layer was roll-printed onto the PEDOT:PSS layer, and the LiF/Al electrode was then evaporated. The thickness of the active layer was fixed at 250 nm, and the active area of the cells was 1.3 cm^2. Figure 9a exhibits the J–V curves of the conventionally annealed solar cells. The bending radius (r) was ∞, 6.7, 2.1, and 1.1 mm, which correspond to bending strain level of ε = 0, 1.3, 4.3, and 8.3% in that order. The bending strain was calculated from the relationship $\varepsilon = (T/2r) \times 100\%$, where T is the device thickness.[51] The device characteristics are summarized in Table 4. A significant decrease

Table 4. Representative Photovoltaic Properties of P3HT Nanofibril–PCBM Blended Films (Photoactive Layer) as a Function of the Bending Radius

type of film	bending radius (mm)	V_{oc} [V]	J_{sc} [mA/cm^2]	FF [%]	PCE [%]
conventional	0	0.55	−5.76	43	1.36
	6.7	0.55	−5.57	42	1.29
	2.1	0.55	−4.97	37	1.00
	1.1	0.55	−4.48	31	0.76
C&H	0	0.55	−7.46	53	1.66
	6.7	0.56	−9.51	51	1.55
	2.1	0.53	−9.81	54	1.44
	1.1	0.55	−10.10	51	1.41

in the PCE was noted at a bending radius of 2.1 mm (ε = 4.3%). The large drop is attributed to crack propagation in the active layer under bending strain, as shown in the SEM image in Figure 9b. Because the deformation and cracks were irreversible in the conventional solar cells, the initial PCE was not recovered after the strain was relieved when the bending radius was larger than 6.7 mm ($\varepsilon \geq$ 1.3%). The photovoltaic performance of the nanofibril-based solar cells showed less dependence on the bending strain (Figure 9c). At a bending radius of 1.1 mm (ε = 8.3%), the PCE remained at 84.9% of its initial value. The decrease of the PCE is regarded the decrease in the projected area of the illumination onto the device surface. In contrast to the conventional films, PCE was reversible upon strain. This type of enhanced stability of nanofibril-based solar cells is attributed to their curvy structure. No cracks or apparent defects were observed at a bending radius of 1.08 mm. A SEM image of the film in a bent state is shown in Figure 9d. The device reliability was examined by repeated bending tests at three bending radii (r = 6.7, 2.1, and 1.1). Figure 9 presents the results from the conventional solar cell (e) and the nanofibril-based solar cell (f). The values represent the PCE after relieving the strains. The PCE of the conventional solar cells sharply dropped as the number of bends increased, whereas the nanofibril-based solar cells showed improved stability during the repeated bending test.

However, it is notable that highly flexible photovoltaic cells can be produced only with flexible cathodes and anodes. The Au/PEDOT:PSS electrode showed clear defect lines at r = 2.1 (ε = 4.3%) (Figure S4). The LiF/Al electrode was weaker against the strain, crazing even at large bending radius (r = 6.7, ε = 1.3%) (Figure S4). In order to compare the strain stability of the BHJ films themselves, the spin-coated films on a Si wafer was transferred to a PDMS-coated PET substrate, and then the repeated bending test was conducted 500 times at the three

bending radii (r = 6.7, 2.1, and 1.1 mm). The bending-tested films were transferred onto a ITO/PEDOT:PSS-coated substrate, and then the LiF/Al electrode was evaporated on the BHJ films. In order to compare the net effect of repeated bending, we prepared reference samples following the same process except for conducting the bending events. The results are seen in Figure 9e,f as solid symbols for r = 6.7 mm (■), r = 2.1 mm (●), and r = 1.1 mm (▲). The PCE values obtained from the bent BHJ layer were normalized by the PCE of their corresponding unbent BHJ films. Severe drop of the PCE was observed in the conventional films. Meanwhile, the PCE in the nanofibril-based solar cells showed a negligible change at the bending radius r = 6.7 and 2.1 mm, and slight degradation was observed at r = 1.1 mm. These results imply that the nanofibrils effectively relieved the mechanical stress.

The photovoltaic performance must be sustainable at high temperatures. Figure 10 shows the change in the PCE over time
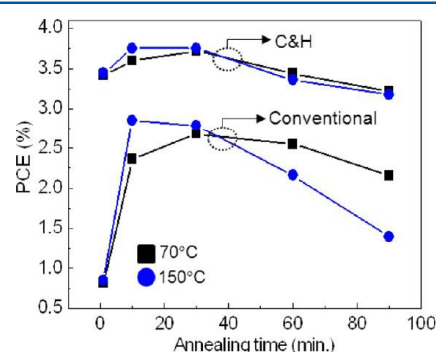

Figure 10. Thermal stability test of solar cells prepared by the conventional annealing process and by the C&H process. The test was conducted at 70 and 150 °C in a N$_2$ environment to exclude other effects.

at different temperatures (70 and 150 °C). Thermal annealing was performed in an N$_2$ environment before the cathode (LiF/Al) was deposited so as to remove the effect of oxidation of the cathode on the photovoltaic performance. The PCE value of the conventional film devices was increased by annealing for 10–20 min at both annealing temperatures, but the PCE after annealing at 150 °C sharply decreased as the annealing time increased. The nanofibril-based solar cells showed a small increase in the PCE, which then started to decrease during the annealing process. However, the rate of decrease was lower than those of the conventional film cells. More importantly, the results after annealing at 150 °C did not differ from those at 70 °C. The enhanced thermal stability of the BHJ layer is attributed to the network structure of the long P3HT nanofibrils, which prevents the of PCBM phase from being phase-separated into microscale particles.[34,41,56]

■ **CONCLUSION**

We applied a cooling-and-heating (C&H) cycle to a P3HT/PCBM solution and prepared P3HT:PCBM bulk heterojunction layers consisting of long P3HT nanofibrils with nearly 100% crystallinity. The fast hole transport in the thickness direction of the nanofibril-based BHJ layers provided more tolerance at the optimum thickness of the photoactive layer. We found that the photoconversion efficiency (PCE) of the nanofibril-based solar cells remained the same within a broad thickness range of 100–500 nm, which is in the controllable

range used with current printing technologies. In addition, the enhanced hole mobility enabled the fabrication of large-area unit cells (10.5 cm^2) that retained 63% of their power conversion efficiency in small cells (5.4 mm^2), whereas the efficiency of the conventional cells fell to less than 20% of the PCE in small cells. We utilized the roll-printing in the air to take advantage of the improved device conditions. The wavy contour path of the nanofibrils effectively absorbed the external strain. The conversion efficiency of the conventional BHJ cells largely decreased as the bending radius was narrowed and abruptly dropped as the number of bends increased. Under a large amount of strain ($\varepsilon = 8.3\%$), cracks propagated in the conventional cells and PCE became meaningless, whereas the nanofibril-based solar cells showed greatly enhanced stability against the bending. Owing to the nearly 100% crystallinity of the P3HT nanofibrils, the nanofibril-based solar cells exhibited excellent thermal stability. The advantages simply obtained with the cool-and-heat process for the polymer solution enables the continuous printing of large-area organic solar cells without thermal annealing.

■ EXPERIMENTS AND METHODS

Device Fabrication. Solar cells were fabricated on indium tin oxide (ITO)-coated glass. The ITO glass was consecutively cleaned with trichloroethylene, acetone, and isopropyl alcohol and was then treated with UV-ozone for 30 min. A thin film of poly(3,4-ethylenedioxythiophene)−poly(styrenesulfonate) (PEDOT:PSS, 40 nm thickness, Baytron P, Bayer AG) was spin-coated onto the glass and was then annealed at 140 °C in air. Regioregular P3HT ($M_w = 50$ 000, RR > 95%) and PCBM (phenyl-C$_{61}$-butyric acid methyl ester) were purchased from Reike Metal and Nano C, respectively. The 1D crystal seeds of the P3HT were generated by a cycle of cooling-and-heating a blended solution (P3HT:PCBM 1:1 w/w, 2 wt % in *m*-xylene).[39] The solution was cooled in a chiller at −15 °C for 15 min and then heated to room temperature (25 °C) in air. The thin BHJ films were prepared by spin-coating, following a previously published process.[39] A roll-printing process was used for the large-area thick BHJ films. A small roller of the type typically used for painting was dipped in the P3HT:PCBM solution containing the P3HT crystal seeds. We painted with the roller directly onto the PEDOT:PSS layer. The samples were dried in air for 1 h to remove the residual solvent. Metal top electrodes (LiF: 0.8 nm/Al: 100 nm) were deposited on the photoactive layer by thermal evaporation under a high vacuum (low 10^{-6} Torr). Flexible solar cells were fabricated on the Au-deposited (10 nm) d-poly(ethylene terephthalate) (PET) substrate instead of an ITO layer. The process described above was employed.

Device Characterization. The performance of the solar cells was characterized under AM 1.5 solar illumination at an intensity level of 100 mW/cm^2. The measurement was conducted by a Keithley 236 source meter and an Oriel 300 W solar simulator in air within 1 h after the devices were exposed to air. The UV−vis absorbance spectra of the solutions and the BHJ films were obtained with a Jasco V-570 spectrophotometer. The morphology of the photoactive layers was investigated by an atomic force microscope (AFM, Asylum Research MFP-3D-SA) in tapping mode, a scanning electron microscope (SEM, JEOL JSM-7001F), and a transmission electron microscope (TEM, JEOL JEM-2011HC) operated at 120 kV. The analysis of the P3HT crystal structure was performed by X-ray diffraction (XRD, Rigaku Ultima IV). The thickness of the films was measured using an ellipsometer (Nano view, SE MG-1000 Vis) and a surface profiler (KLA-Tencor, AS500).

■ ASSOCIATED CONTENT

ⓢ Supporting Information

UV−vis absorbance spectra of photoactive solutions; SEM images of the electrodes after mechanical bending. This material is available free of charge via the Internet at http://pubs.acs.org.

■ AUTHOR INFORMATION

Corresponding Author

*E-mail: ujeong@yonsei.ac.kr (U.J.); thinfilm@yonsei.ac.kr (H.K.B.).

Notes

The authors declare no competing financial interest.

■ ACKNOWLEDGMENTS

■ REFERENCES

(1) McNeill, R.; Siudak, R.; Wardlaw, J. H.; Weiss, D. E. *Aust. J. Chem.* **1963**, *16*, 1056−1075.

(2) Shirakawa, H.; Louis, E. J.; MacDiarmid, A. G.; Chiang, C. K.; Heeger, A. J. *J. Chem. Soc., Chem. Commun.* **1977**, *16*, 578−580.

(3) Koezuka, H.; Tsumura, A.; Ando, T. *Synth. Met.* **1987**, *18*, 699−704.

(4) Coakley, K. M.; McGehee, M. D. *Chem. Mater.* **2004**, *16*, 4533−4542.

(5) Oh, J. Y.; Jang, W. S.; Lee, T. I.; Myoung, J.-M.; Baik, H. K. *Appl. Phys. Lett.* **2011**, *98*, 023303.

(6) Schilinsky, P.; Waldauf, C.; Brabec, C. J. *Appl. Phys. Lett.* **2002**, *81*, 3885.

(7) Li, G.; Shrotriya, V.; Huang, J.; Yao, Y.; Moriarty, T.; Enery, K.; Yang, Y. *Nat. Mater.* **2005**, *4*, 864−868.

(8) He, M.; Qiu, F.; Lin, Z. *J. Mater. Chem.* **2011**, *21*, 17039−17048.

(9) He, M.; Han, W.; Ge, J.; Yang, Y.; Qiu, F.; Lin, Z. *Energy Environ. Sci.* **2011**, *4*, 2894−2902.

(10) He, M.; Zhao, L.; Wang, J.; Yang, Y.; Qiu, F.; Lin, Z. *ACS Nano* **2010**, *6*, 3241−3247.

(11) Li, G.; Zhu, R.; Yang, Y. *Nat. Photonics* **2012**, *6*, 153−161.

(12) Service, R. *Science* **2011**, *332*, 293.

(13) Scharber, M. C.; Műhlbacher, D.; Koppe, M.; Denk, P.; Waldauf, C.; Heeger, A. J.; Brabec, C. J. *Adv. Mater.* **2006**, *18*, 789−794.

(14) Forrest, S. R. *Nature* **2004**, *428*, 911−918.

(15) Krebs, F. C. *Sol. Energy Mater. Sol. Cells* **2009**, *93*, 394−412.

(16) Krebs, F. C. *Org. Electron.* **2009**, *10*, 761−768.

(17) McCulloch, I.; Heeney, M.; Bailey, C.; Genevicius, K.; MacDonald, I.; Shkunov, M.; Sparrowe, D.; Tierney, S.; Wagner, R.; Zhang, W.; Chabinyc, M. L.; Kline, R. J.; McGehee, M. D.; Toney, M. F. *Nat. Mater.* **2006**, *5*, 328−333.

(18) Moulé, A. J.; Meerholz, K. *Adv. Mater.* **2008**, *20*, 240−245.

(19) Padinger, F.; Rittberger, R. S.; Sariciftci, N. S. *Adv. Funct. Mater.* **2003**, *13*, 85−88.

(20) Yang, X.; Loos, L.; Veenstra, S. C.; Verhees, W. J. H.; Wienk, M. M.; Kroon, J. M.; Michels, M. A. J.; Janssen, R. A. J. *Nano Lett.* **2005**, *5*, 579−583.

(21) Ma, W.; Yang, C.; Heeger, A. J. *Adv. Mater.* **2007**, *19*, 1387−1390.

(22) Jo, J.; Kim, S.-S.; Na, S.-I.; Yu, B.-K.; Kim, D.-Y. *Adv. Funct. Mater.* **2009**, *19*, 866−874.

(23) Campoy-Quiles, M.; Ferenczi, T.; Agostinelli, T.; Etchegoin, P. G.; Kim, Y.; Anthopoulos, T. D.; Stavrinou, P. N.; Bradley, D. D. C. *Nat. Mater.* **2008**, *7*, 158−164.

(24) Xu, Z.; Chen, L.-M.; Yang, G.; Huang, C.-H.; Hou, J.; Wu, Y.; Li, G.; Hsu, C.-S.; Yang, Y. *Adv. Funct. Mater.* **2009**, *19*, 1227−1234.

(25) JØrgensen, Z. M.; Norrman, K.; Krebs, F. C. *Sol. Energy Mater. Sol. Cells* **2008**, *92*, 686−714.

(26) Müller, C.; Ferenczi, T. A. M.; Campoy-Quiles, M.; Frost, J. M.; Bradley, D. D. C.; Smith, P.; Stingelin-Stutzmann, N.; Nelson, J. *Adv. Mater.* **2008**, *20*, 3510−3515.

(27) Hintz, H.; Egelhaaf, H.-J.; Lüer, L.; Hauch, J.; Peisert, H.; Chasse, T. *J. Appl. Phys.* **2009**, *106*, 034506.

(28) Baek, W.-H.; Yoon, T.-S.; Lee, H.-H.; Kim, Y.-S. *Org. Electron.* **2010**, *11*, 933−937.

(29) Li, L.; Lu, G.; Yang, X. *J. Mater. Chem.* **2008**, *18*, 1984−1990.

(30) Berson, S.; Bettignies, E. D.; Bailly, S.; Guillerez, S. *Adv. Funct. Mater.* **2007**, *17*, 1377−1384.

(31) Kim, J.-H.; Park, J. W.; Lee, J. H.; Kim, J. S.; Sim, M.; Shim, C.; Cho, K. *J. Mater. Chem.* **2010**, *20*, 7398−7405.

(32) Kim, J. S.; Lee, J. H.; Park, J. H.; Shim, C.; Sim, M.; Cho, K. *Adv. Funct. Mater.* **2011**, *21*, 480−486.

(33) Xin, H.; Kim, F. S.; Jenekhe, S. A. *J. Am. Chem. Soc.* **2008**, *130*, 5424−5425.

(34) Wu, P.-T.; Xin, H.; Kim, F. S.; Ren, G.; Jenekhe, S. A. *Macromolecules* **2009**, *42*, 8817−8826.

(35) Xin, H.; Reid, O. F.; Ren, G.; Kim, F. S.; Ginger, D. S.; Jenekhe, S. A. *ACS Nano* **2010**, *4*, 1861−1872.

(36) Ren, G.; Wu, P.-T.; Jenekhe, S. A. *ACS Nano* **2011**, *5*, 376−384.

(37) Byun, M.; Laskowski, R. L.; He, M.; Qiu, F.; Jeffries-EL, M.; Lin, Z. *Soft Mater.* **2009**, *5*, 1583−1586.

(38) Han, W.; He, M.; Byun, M.; Li, B.; Lin, Z. *Angew. Chem., Int. Ed.* **2013**, *52*, 2564−2568.

(39) Oh, J. Y.; Shin, M.; Lee, T. I.; Jang, W. S.; Min, Y.; Myoung, J.-M.; Baik, H. K.; Jeong, U. *Macromolecules* **2012**, *45*, 7504−7513.

(40) Park, Y. D.; Lee, H. S.; Choi, Y. J.; Kwak, D.; Cho, J. H.; Lee, S.; Cho, K. *Adv. Funct. Mater.* **2009**, *19*, 1200−1206.

(41) Oh, J. Y.; Lee, T. I.; Myoung, J.-M.; Jeong, U.; Baik, H. K. *Macromol. Rapid Commun.* **2011**, *32*, 1066−1071.

(42) Abbas, M.; Tekin.. *Appl. Phys. Lett.* **2012**, *101*, 073302.

(43) Shieh, J.-T.; Liu, C.-H.; Meng, H.-F.; Tseng, S.-R.; Chao, Y.-C.; Horng, S.-F. *J. Appl. Phys.* **2010**, *107*, 084503.

(44) Jung, J. W.; Jo, W. H. *Adv. Funct. Mater.* **2010**, *20*, 2355−2363.

(45) Servaites, J. D.; Yeganeh, S.; Marks, T. J.; M., A.; Ratner, M. A. *Adv. Funct. Mater.* **2010**, *20*, 97−104.

(46) Pandey, A. J.; Nunzi, J.-M. *Appl. Phys. Lett.* **2011**, *99*, 093309.

(47) Choi, S.; Potscavage, W. J.; Kippelen, B. *J. Appl. Phys.* **2009**, *106*, 054507.

(48) Yeo, J.-S.; Yun, J.-M.; Kim, S.-S.; Kim, D.-Y.; Kim, J.; Na, S.-N. *Semicond. Sci. Technol.* **2011**, *26*, 034010.

(49) Sokolov, A. S.; Cao, Y.; Johnson, O. B.; Bao, Z. *Adv. Funct. Mater.* **2012**, *22*, 175−183.

(50) Bensaid, B.; Boddaert, X.; Benaben, P.; Gwoziecki, R.; Coppard, R. *Eur. Phys. J. Appl. Phys.* **2011**, *55*, 23907.

(51) O'Connor, B.; Chan, E. P.; Chan, C.; Conrad, B. R.; Richter, L. J.; Kline, R. J.; Heeney, M.; McCulloch, I.; Soles, C. L.; DeLongchamp, D. M. *ACS Nano* **2010**, *4*, 7538−7544.

(52) Park, S. K.; Kim, Y. H.; Han, J. I.; Moon, D. G.; Kim, W. K. *Thin Solid Films* **2003**, *429*, 231−237.

(53) Kim, J. B.; Kim, P.; Pègard, N. C.; Oh, S. J.; Kagan, C. R.; Fleischer, J. W.; Stone, H. A.; Loo, Y.-L. *Nat. Photonics* **2012**, *6*, 327−332.

(54) Lipomi, D. J. B.; Tee, C.-K.; Vosgueritchian, M.; Bao, Z. *Adv. Mater.* **2011**, *23*, 1771−1775.

(55) Tahk, D.; Lee, H. H.; Khang, D.-Y. *Macromolecules* **2009**, *42*, 7079−7083.

(56) Lin, C.; Lin, E.-Y.; Tsai, F.-Y. *Adv. Funct. Mater.* **2010**, *20*, 834−839.